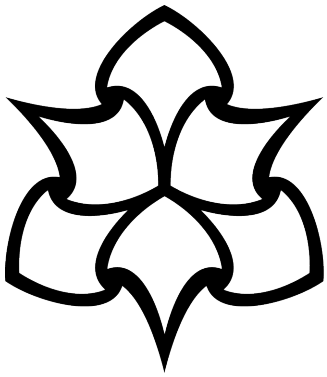

energies

MDPI

Article

# Performance Assessment and Improvement of Central Receivers Used for Solar Thermal Plants

**Alhussein Albarbar * and Abdullah Arar**

Advanced Industrial Diagnostic Research Centre, School of Engineering, Manchester Met University, Manchester M1 5GD, UK

* Correspondence: a.albarbar@mmu.ac.uk

Received: 25 June 2019; Accepted: 5 August 2019; Published: 9 August 2019


**Abstract:** In this work, the energy status and supply plans of Saudi Arabia are discussed with a focus on concentrated solar power (CSP) technologies. Subsequently, optimal designs for a 20 MWe solar power plant external receiver, combined with a 15 h thermal energy storage unit, operating under the weather conditions of Neom City, located in northeast Saudi Arabia, is proposed. The effects of receiver tube diameters, tube thicknesses, tube thermal conductivity and receiver's performance are studied in detail and compared to those used in a well know operational CSP plant. Results show that a smaller tube diameter and thickness give higher receiver thermal efficiency but increase the annual cost of pumping energy. However, that increment in cost is negligible compared to the total energy gained. Furthermore, the aspect ratio is investigated and it was found that a higher aspect ratio gives a higher thermal efficiency. The thermal efficiency of the optimised receiver was increased by about 1% more than the reference plant. In addition, the new design decreases the total estimated cost of tube material by approximately 43%. It is anticipated that the reported results could pave the path for more efficient solar thermal power plants.

**Keywords:** solar energy; solar power thermal plant; central receiver; design; solar energy in Saudi Arabia

## 1. Introduction

At present, as in most parts of the world, conventional electric power generation is the main source of electricity in Kingdom of Saudi Arabia (KSA). It is also expected the demand for electricity in KSA will increase from 55 GW to about 121 GW by 2032, with a gap of 61 GW between the capacity of projected plants and the predicted demand [1].

Therefore, more attention should be given to renewable energy generation technologies. The recently announced energy mix plan in KSA for 2032 is shown in Figure 1 [1]. The plans aim to produce around 45% (54 GW) of its electricity demand from renewable sources, including 25 GW from CSP technology, 16 GW from photovoltaic solar cells, 9 GW through wind turbine technology, 4 GW by using geothermal and waste-to-energy technology. In Saudi Arabia (where the sky is often clear around the year), the average yearly direct solar radiation is more than 2000 kWh/m$^2$/year which makes concentrated solar power (CSP) promising renewable technologies that can boost the country's energy mix [1].

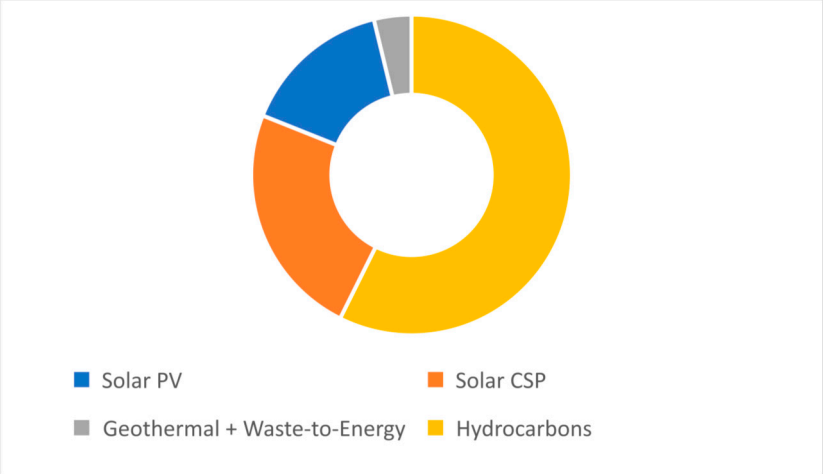


**Figure 1.** Renewable energy mix plan in [GW] of Saudi Arabia for 2032 [1].

CSP technologies can be categorised according to the type of solar collector into four main technologies: parabolic trough concentrator (PTC), linear Fresnel reflector (LFR), dish Stirling and solar power tower (SPT). Figure 2 illustrates a schematic diagram for each technology [2].

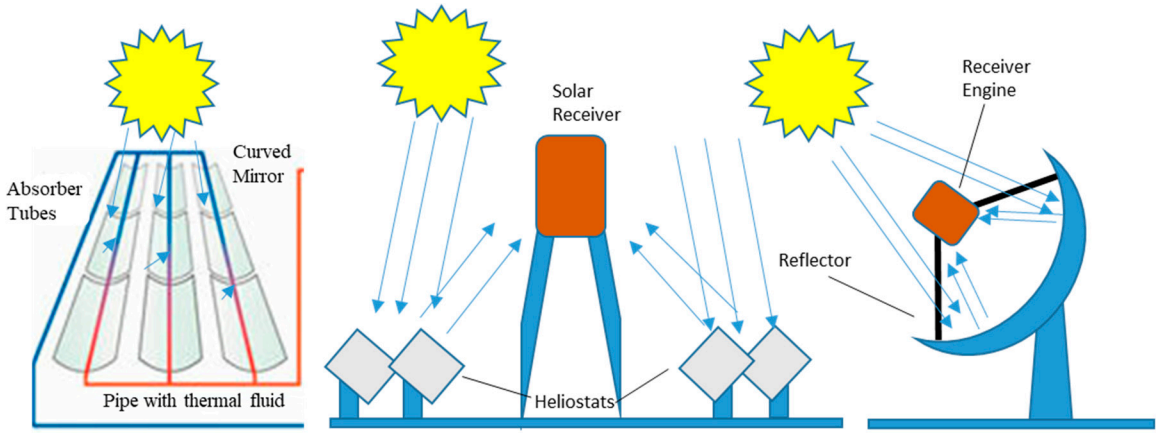


**Figure 2.** The main technologies of concentrated solar power systems.

Direct normal irradiance (DNI) represents the portion of solar radiation reaching the Earth's surface that has not been diffused or scattered by the atmosphere. In Saudi Arabia, the average yearly DNI varies between a maximum of 2400 kWh/m$^2$/day at the western inland sites of the kingdom to a minimum of 2000 kWh/m$^2$/day at the eastern regions of the kingdom. Therefore, this technology could be the best alternative renewable energy system for the country, which could boost the 2032 energy mix plan [1], reduces pollutions and meet the energy demands of the new projects such as Neom City in the northeast of KSA. Another advantage for using CSP technology in the KSA is its ability of adding thermal energy storage (TES) subsystem to the plant. Due to the variability of the solar resource energy, e.g., the PV cell cooperates with a battery storage units, has limited storage capacity and degrade over the time of usage. However, CSP plant can use large thermal energy storage (TES) units, which the capability to work at a full-rated capacity for hours—even after the absence of solar energy.

SPT technology consists of four main subsystems: a heliostat field subsystem, central receiver subsystem, thermal energy storage (TES) subsystem and power generation subsystem. Design optimisation of the central receiver subsystem has a great impact on the total efficiency of a solar power plant. However, defining the optimum design in terms of the outer and inner geometry of a receiver is one of the challenges associated with designing SPT plants. Li et.al. developed a global steady state

mathematical model for a 100 kWth cavity receiver [3]. Molten salt was used as the heat transfer fluid (HTF), and the influence of the receiver surface area, the emissivity and reflectivity of the receiver surface, the view factor, the number of tubes on the receiver panel and the optimal tube diameter for the thermal performance of the cavity receiver were investigated. Convection heat loss comprises the largest part of the total heat losses for a cavity receiver because both the natural and forced convective heat loss rates are included.

Yang et al. examined the characteristics of receiver tubes to determine their effect on the performance of a central receiver [4]. The outcome of the experiment indicated that, compared to smooth tubes, spiral tubes can reduce convection and radiation heat losses and improve the total efficiency of the receiver. The study also showed that the Nusselt number for a spiral tube is about three times that of a smooth one. As a result, the surface temperature of a spiral tube is lower than that of a smooth tube by approximately 30 °C, which leads to less heat loss.

Rodriguez-Sanchez et al. designed a new external central receiver formed by several vertical bayonet tubes [5]. Under the same ambient conditions, a numerical simulation model was developed to compare the performance of the new design with the traditional external tubular receiver. This work showed that using a bayonet tube receiver can increase the efficiency of the receiver by about 2% and the receiver surface temperature of the bayonet receiver fell by around 100 °C. However, bayonet tubes could make the wall temperature more homogeneous. Consequently, the thermal stresses would decrease, which reduces the early failure of the receiver due to fatigue.

The effect of using transparent insulation materials to enhance the thermal performance of a central receiver was studied in [6]. The performance of an external cylindrical receiver was analysed by integrating a glass envelop layer plus a transparent insulation marital layer into the design. The result of this work showed, in general, that using the insulation material at a low receiver surface temperature (<484 °C) provides low receiver efficiency, and it is better to use the traditional receiver without any insulation material. The benefit of the insulation becomes clear at high-operation work temperatures (>600 °C).

Using a flat-plate receiver, with a 13 kWth thermal energy capacity, a prototype SPT system was designed and tested under the weather conditions of Jeddah (KSA) [7]. Molten salt was used as the HTF and thermal storage material. Ten mirrors with a total surface area of 17.2 $m^2$ were installed in the heliostat field area. The prototype showed that Jeddah is an appropriate site to construct a central tower solar plant. Benoit et al. discussed current and future heat transfer fluids and heat storage mediums, which can be utilized in the external solar receiver [8]. They also presented various thermo-physical properties correlations to determine the heat transfer coefficient. It was concluded that current HTFs can achieve thermodynamics efficiency of up to 35% to 42%. This efficiency could reach 50% using new molten salt that ensures supercritical water thermal stability up to 700 °C. In [9], Zheng et al. demonstrated that raising the receiver working temperature could initially increase both thermal and exergy conversion efficiencies until an optimum temperature is reached. They also found that increasing the concentration ratio could raise the conversion efficiency until the concentration ratio is extremely high. Wang et al. presented a model for molten salt solar power tower (SPT) system integrated with a S-$CO_2$ Brayton cycle [10]. System costs change with the types of storage tanks and also that the operation temperature is limited by the thermal properties of the thermal storage medium [11]. The findings also stated that cost of energy can be substantially reduced by replacing the conventional power cycle with more advanced power cycles, such as a supercritical carbon dioxide power cycle [11]. Potential freezing of the HTF in the system has been addressed by Prieto et al. [12]. Two methods of freeze recovery have been presented: heat tracing in pipes and components, and impedance melting in the solar field. The models compare the parasitic consumption in three molten salts mixtures, namely Solar Salt, HiTec, and HiTec XL, under freezing conditions. Results show freeze recovery for a molten salt plant is possible.

In addition to an updated overview on energy plans for KSA, the paper proposes optimal design for cylindrical receiver, including its performance assessment, under the meteorological conditions

of Neom city in Saudi Arabia. The rated and thermal storage capacities of the proposed solar tower system are 20 MWe and 15 h, respectively. The main two aspects used to define the optimum geometry are as follows: the receiver thermal efficiency and the annual cost of the receiver pumping energy.

## 2. Status of Concentrated Solar Power (CSP)

At present, the majority of the installed CSP plants are either parabolic trough concentrator (PTC) or solar power tower (SPT) designs [5]. In the PTC system, a parabolic shape collector (reflector) is used to reflect sunlight onto an absorber (receiver), which is usually made from a metal tube and then enclosed in a glass tube to reduce the radiation and convection heat losses. In addition, a vacuum between the glass tube and the absorber is introduced to minimise the convection heat losses. To reach the desired temperature (max ≈ 550 °C), the heat transfer fluid (HTF) needs to be pumped into series of parabolic collectors that are connected to each other [3].

An SPT system (also known as a central receiver tower) consists of four major subsystems: a heliostat field, central receiver subsystem, thermal storage subsystem and power generation subsystem. In SPT, large mirrors called heliostats, which have a reflective surface area range from 50 to 150 $m^2$, are arranged in a solar field to reflect and concentrate incident solar radiation to a central receiver located at the top of a supporting tower. The receiver consists of tubes through which the HTF flows, heated up from 590 °C to 1000 °C depending on the central receiver geometry and the thermal specification of the HTF. Then, the absorbed thermal energy is transported either to a power generation subsystem or to a thermal storage subsystem. The aim of the thermal storage system is to allow the solar power system to produce electric power in the absence of solar radiation, as shown in Figure 3 [13].

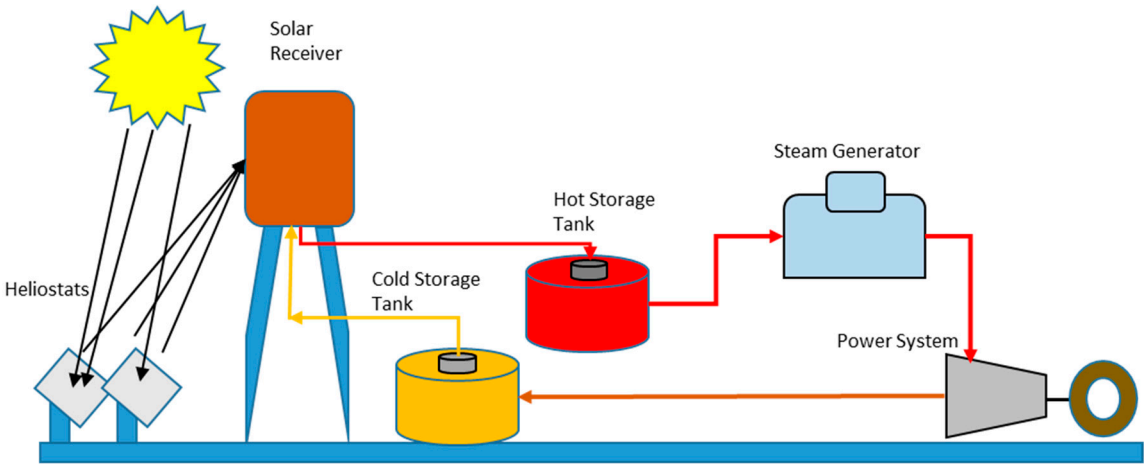


**Figure 3.** Solar power tower plant subsystems [12].

A solar tower has number of advantages that could make this technology the most preferable CSP method. The main potential advantages are summarised as follows:

- In a solar tower system, the HTF can be heated up to 1000 °C, which yields to a larger thermal-to-electric conversion efficiency in the power block subsystem and can result in a lower cost of generating power.
- The higher temperature of the HTF allows the solar system to store the exceeded thermal energy in a thermal storage system, which can give the solar system the ability to operate longer.

Despite PTC technology having the most commercial operating plants, as depicted in Figure 4, the SPT system has gained a lot of interest recently, and the construction and development of this type of solar system is a growing trend [14].

In Saudi Arabia, the development of CSP technologies is as advanced as those of the leaders of other Sun Belt countries. In 2017, the Saudi government lunched two natural gas combined cycle-CSP

hybrid plants. Both plants use PTC technology. The first project is located on the western coast of the country in Duba. The projected capacity of the plant is 565 MWe. Around 43 MWe of the projected capacity is generated by the PTC technology. The second project is in a new industrial city close to the northern border of the country. The project, called Waad Al Shamal, aims to generate a total output of 1390 MWe, of which 50 MWe produced by PTC technology. So far, in Saudi Arabia, SPT technology has not been used in a commercial power plant. However, a recent trend of using SPT is apparent due to new projects in several countries, such as Noor III (150 MWe) in Morocco, Redstone in South Africa (100 MWe) and DEWA in the United Arab Emirates (200 MWe). Plans also include Seih Al-Dahal, the area of 48 $km^2$ is enough to construct plants (PV and CSP) with a total capacity of 1000 MW by 2030 [15]. Therefore, SPT may be a strong choice for generating electricity for KSA in the coming years.

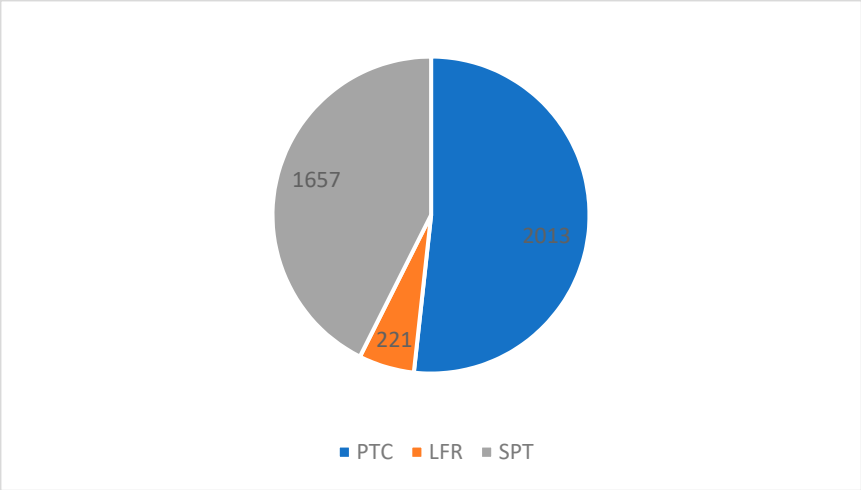


**Figure 4.** Solar power projects under construction or development [14].

## 3. Modelling of CSP Central Receiver

### *3.1. Equivalent Capacity of the System*

To determine the amount of incident thermal energy on the central receiver ($Q_{re}$), rated capacity (the required net electric output power) of the proposed SPT system and thermal energy capacity of the TES subsystem are required. The combination of these capacities forms the equivalent capacity of a solar power plant. It is assumed that a typical solar power plant without thermal storage can generate electric power for nine hours. Further, the equivalent capacity for a SPT system with (x) hour's thermal energy storage capacity is defined in Equation (1):

$$\text{Equivalent capacity} = \text{Rated capacity} \times \frac{(9 + x)}{9}. \quad (1)$$

The efficiency of a heliostat field subsystem, central receiver subsystem and power block subsystem are assumed to be 70%, 85% and 42%, respectively [6]. Then, the total efficiency of the SPT system can be calculated by Equation (2):

$$\eta_{total} = \eta_{opt} \times \eta_{re} \times \eta_{tur}. \quad (2)$$

### *3.2. Direct Normal Irradiance (DNI)*

To design a solar tower system, it is important to define a design point at which the solar system will run at full capacity. Since environmental solar radiation varies over time, it is necessary to decide on a point when the device will reach peak performance. This time was chosen to be mid-day and was used to define the optimum design point of the system. During this time, solar radiation DNI

commonly reaches the highest concentration. Figure 5 depicts the available free hourly DNI data for the North East of KSA.

This study used a histogram chart to find the most frequent DNI over the year. The histogram chart, in Figure 6, shows that the most frequent value of DNI is 950 W/m$^2$, 1000 and 50 W/m$^2$ are the second highest frequent value of DNI. However, the 50 W/m$^2$ represents the solar radiation at the early and last hours of a day, which are usually neglected in designing a solar system.

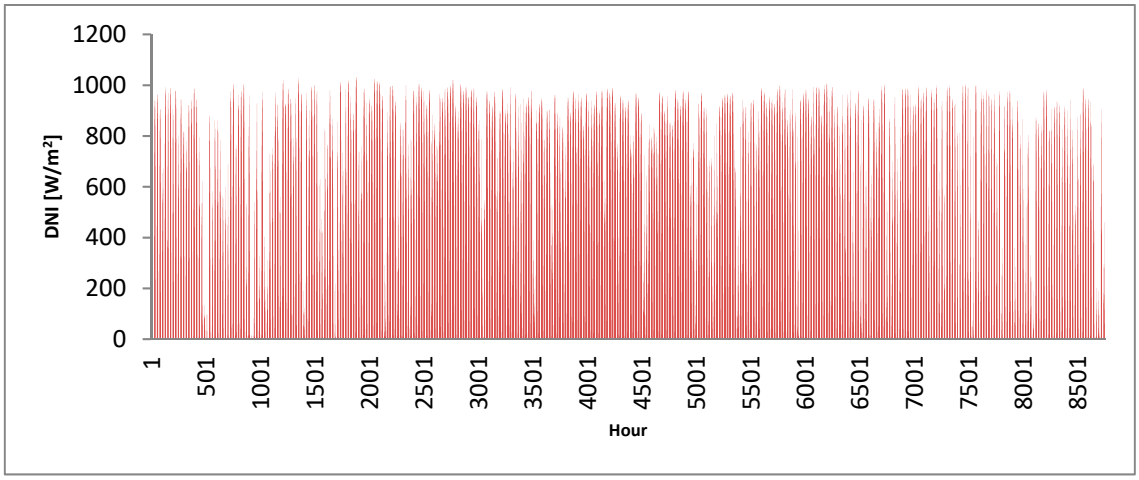


**Figure 5.** Hourly direct normal irradiance (DNI) for the region (www.soda-pro.com).

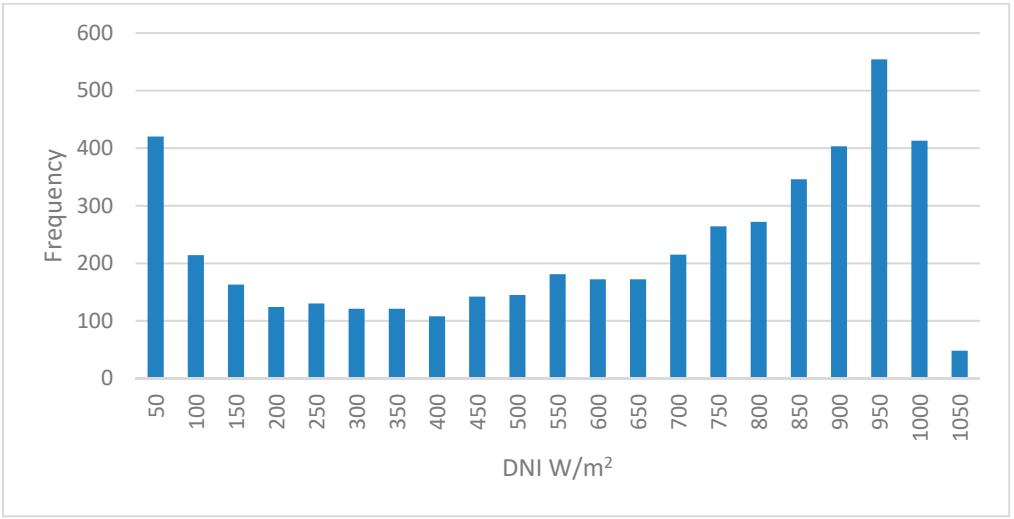


**Figure 6.** A histogram chart for DNI in the region.

### *3.3. Determination of Heliostat's Reflecting Area*

To estimate the useful active reflecting area of the heliostat field ($A_h$), the required thermal energy needed to be reflected by the heliostat field to the central receiver has to be determined. This can be calculated using Equation (3):

$$Q_h = \frac{\text{Equivalent capacity}}{\eta_{opt} \times \eta_{re} \times \eta_{tur}} \quad (3)$$

Then, the heliostat-reflecting area ($A_h$), m$^2$ is calculated by Equation (4):

$$A_h = \frac{Q_h}{DNI}, \quad (4)$$

where $Q_h$ is the thermal energy that needs to be reflected by the heliostat field subsystem (in W) and DNI is the solar radiation per unit surface area (in W/m$^2$).

### *3.4. Receiver Thermal Energy*

Since the design point of solar radiation DNI and the total useful reflecting area of the heliostat field have been calculated, the total incident thermal energy on the central receiver can be computed. $Q_{re}$ can be expressed using Equation (5):

$$Q_{re} = DNI \times A_h \times \eta_h \quad (5)$$

where $Q_{re}$ is the total incident thermal energy on the receiver W/m$^2$ and $\eta_h$ is the heliostat field efficiency.

### *3.5. Proprieties of Heat Transfer Fluid*

The thermal properties of molten salt (60% wt $NaNO_3$ and 40% wt $KNO_3$) play a major role in designing a central receiver. These properties can define the operating temperature of a central receiver. For example, the melting temperature for a molten salt HTF (temperature for the transition 100% solid into solid + liquid) is 221 °C, and the freezing temperature (temperature for the transition 100% liquid into solid + liquid) is 238 °C. Therefore, the minimum operating temperature of molten salt has been defined as 290 °C to avoid any transition of molten salt into a solid phase inside the receiver tubes, which could damage the receiver. In addition, the maximum operating temperature is also important to avoid any decomposition of the solar salt, which begins at about 580 °C [16]. The molten salt from is pumped to the receiver from cold tank, with the temperature of the molten salt at 290 °C then heated up to 565 °C by the thermal energy of solar radiation impinging on the receiver surface. mean temperature of the HTF is calculated by Equation (6) [17]:

$$T_{ms} = (T_{in,ms} + T_{out,ms})/2 \quad (6)$$

where $T_{in,ms}$ and $T_{out,ms}$ are the inlet and outlet temperature of the molten salt (290 °C and 565 °C), respectively. Thermal conductivity of the molten salt can be assumed a constant ($k_{ms}$ = 0.45 W/m·K). Molten salt properties are listed in Table 1.

**Table 1.** Physical proprieties of molten salt [17].

| | |
|---|---|
| Fluid density (ρ), [kg/m$^3$] | $\rho_{ms} = 2263.628 - 0.636 \cdot T_{ms}$ |
| Specific heat capacity, [J/(kg·K)] | $Cp_{ms} = 1396.044 + 0.172 \cdot T_{ms}$ |
| Dynamic viscosity [Pa·s] | $\mu_{ms} = 0.075439 - 2.77 \cdot 10^{-4} \cdot (T_{ms}) + 3.49 \cdot 10^{-7} \cdot (T_{ms})^2 - 1.474 \cdot 10^{-10} \cdot (T_{ms})^3$ |

### *3.6. Calculations of Receiver Outer Geometry*

The outer receiver geometry plays a major role in defining receiver efficiency because it can affect the total thermal heat losses in a receiver. Outer geometry of a receiver includes total receiver surface area ($A_{re}$), receiver height ($H_{re}$) and receiver diameter ($D_{re}$).

#### 3.6.1. Allowable Heat Flux

The calculations associated with the receiver surface area are related to the allowable heat flux. Heat flux can be defined as the rate of heat energy transferred through a meter surface of the receiver. The peak value for the heat flux depends on the thermal stress of a tube's material and the thermal heat capacity of a HTF. From the perspective of the tube's material, the allowable thermal strain, thermal expansion and Poisson's ratio are used to calculate the maximum heat flux for a receiver. For example, the maximum heat flux for a receiver constructed from a 316 stainless steel material ranges from 830 to 850 kW/m$^2$ [17]. Furthermore, in terms of the thermal capacity of the HTF, the flux limit for molten salt ranges from 600 to 1200 kW/m$^2$. As a conservative design approach, peak-to-average heat flux ratio is

used to compute the allowable heat flux on a receiver surface. Using allowable heat flux instead of the peak heat flux would increase the expected lifetime of a receiver because it would reduce the rate of heat energy transfer through the surface of the receiver; in other words, it would reduce the receiver surface temperature. For an external cylindrical receiver using molten salt as a HTF, such as that used by the Gemasolar solar power plant (with a 20 MWe rated capacity), the peak-to-average heat flux ratio is 1.47 [18]. Falcone [19] used a 1.78 peak-to-average heat flux ratio in his design approach for a SPT plant having a rated capacity of 100 MWe. Thermal stress analysis is out of the scope of this work, so the peak-to-average heat flux value of the Gemasolar power plant is used for the current design approach. Thus, the value of the peak-to-average heat flux ratio for in this work was 1.47 and allowable heat flux is described by Equation (7):

$$\text{Allowable heat flux} = \text{Max. heat flux} \times \text{peak to average heat flux ratio} \tag{7}$$

$$\text{Allowable heat flux} = 850[\frac{\text{kW}}{\text{m}^2}] \times 1.47$$

$$\text{Allowable heat flux} = 578.23\ \frac{\text{kW}}{\text{m}^2}.$$

3.6.2. Diameter and Height of Receiver

After determining of total receiver thermal energy ($Q_{re}$) and the allowable heat flux, the receiver surface area ($A_{re}$) can be defined by Equation (8):

$$A_{re} = \frac{Q_{re}}{\text{Allowable heat flux}} \tag{8}$$

where $A_{re}$ is the total receiver surface area ($m^2$). Then, to define the height and diameter of an external receiver, the receiver aspect ratio (height-to-diameter) is assumed to range from 1 to 2 [17]. To find the optimum aspect ratio, a compromise between thermal and spillage losses is required. A taller height receiver is desirable to minimise the thermal heat losses and spillage loss. Alternatively, a larger diameter receiver is required to increase the inner space to accommodate the interior receiver components, such as the header tubes bends, oven header boxes and support structure. For the external cylindrical receiver, the aspect ratio will be between 1.2 and 1.5 [17] and could be calculated by Equation (9):

$$\text{Aspect ratio} = \frac{H_{re}}{D_{re}} \tag{9}$$

The total surface area of the receiver has been calculated in the previous subsection. Then, the receiver surface area can also be expressed by Equation (10):

$$A_{re} = \pi \times D_{re} \times H_{re} \tag{10}$$

where $D_{re}$ and $H_{re}$ are the diameter and the height of the receiver, respectively. To add the aspect ratio (AR) term into the above equation, the receiver area can be rewritten as shown in Equation (11):

$$A_{re} = \pi \times {D_{re}}^2 \times AR \tag{11}$$

Therefore, the receiver diameter ($D_{re}$) and height ($H_{re}$) can be calculated by Equations (12) and (13):

$$D_{re} = \sqrt{\frac{A_{re}}{AR \times \pi}} \tag{12}$$

$$H_{re} = AR \times D_{re} \tag{13}$$

### 3.6.3. Receiver's Inner Geometry

To define the interior geometry of an external receiver, it is important to know the major inner components of the receiver and how the HTF flows inside them. In general, an external receiver consists of number of panels constructed using vertical metal tubes welded side by side to generate the cylindrical shape of the external receiver. These tubes are connected from the bottom and top to headers. Molten salt heat transfer has a high volumetric heat capacity (J/m$^3$ K) that causes a low volume flow rate (m$^3$/s). Therefore, it is advisable to use a multi-pass flow path in a receiver using molten salt. Wagner et al. [20] analysed eight alternative flow paths of the HTF inside the tube receiver. These flow patterns are depicted in Figure 7.

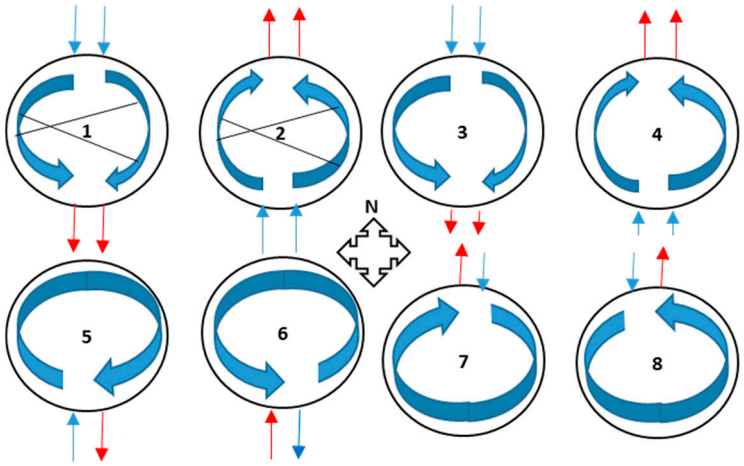


**Figure 7.** Top view for the eight alternative flow patterns of the heat transfer fluid [14].

The study showed that a receiver with two parallel flow paths has higher efficiency than one with a single flow path. Furthermore, the study demonstrated that for a solar site located in the Northern Hemisphere, the south-to-north flow configurations could lead to high receiver efficiency. That is because the solar flux in the Northern Hemisphere is concentrated more on the northern side of the receiver. Therefore, if the cold HTF comes from the north-to-south side of the receiver, the temperature of the HTF and the film temperature of the receiver surface will increase rapidly. As a result, the amount of heat losses are greater than in the south-to-north flow configurations [21]. The present work proposed the North Eastern area of Saudi Arabia as the location of the solar tower system. Thus, the pattern number (4) is used because it has two south-to-north parallel flow paths, which will increase the total efficiency of the solar system.

In the pattern, shown in Figure 8, the HTF (molten salt) is pumped from a cold tank (290 °C) to the top of a tower, where the external receiver is located [3]. At the top of the receiver, the HTF is distributed to two main sides that are usually referred to as the west and east side. Each side of the receiver has number of headers connected to each other in series, and the HTF goes down through the first header to its tubes. Then at the bottom of the tubes, the HTF is collected again and transferred to the next header, which pumps the fluid vertically up insides its tubes. This sequence continues until the last header, where the HTF is collected from the bottom of the receiver. To distribute the number of headers equally to each side of the receiver, it is important that there is an even number of headers per receiver for this type of flow pattern.

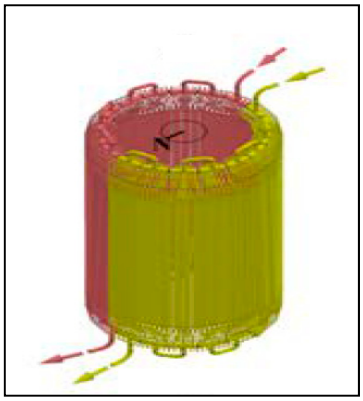

**Figure 8.** Receiver scheme for number 4 flow pattern configuration.

### *3.7. Inner Total Mass Flow Rate*

To simplify the analysis, the total mass flow rate, which describes the mass flow rate inside the main pipe that goes in and out of the external receiver, is assumed to be a constant. In addition to that, the total mass flow rate is related to the amount of thermal energy that is absorbed by the external receiver ($Q_{abs}$ W). The absorbed thermal energy ($Q_{abs}$) is a portion of the total thermal energy received by the receiver. Therefore, the receiver efficiency needs to be assumed so that $Q_{abs}$ can be calculated. The total thermal energy absorbed can be expressed as shown in Equation (14):

$$Q_{abs} = Q_{re} \times \eta_{re}, \tag{14}$$

where $\eta_{re}$ is the receiver thermal efficiency and (as a first assumption) is equal to 85%.

The total mass flow rate $\dot{m}_{total}$ by as shown in Equation (15):

$$\dot{m}_{total} = \frac{Q_{abs}}{Cp \times (T_{out,ms} - T_{in,ms})} \tag{15}$$

where $\dot{m}_{total}$ is the total mass flow rate (kg/s), $Q_{abs}$ is the absorbed thermal energy (W), Cp is the specific heat capacity of the molten salt (J/kg.K), $T_{in,ms}$ is the inlet temperature of the molten salt (K), and $T_{out,ms}$ is the outlet temperature of the molten salt (K).

#### 3.7.1. Number of Tubes and Headers

The size of the outer tube diameter ($d_{out}$) was assumed to range from 20 mm to 56 mm. The tube thickness (t) value depends on the HTF pressure inside the tube. When considering molten salt heat transfer in a solar application, the pressure of the fluid is relatively low and the tube thickness can be as low as 1.25 mm [22]. However, a tube thickness in the range of 1 to 5 mm is used to discern the effect of tube thickness on receiver efficiency. Therefore, the inner diameter is calculated using Equation (16):

$$din = dout - 2 \times t \tag{16}$$

where $d_{out}$ and $d_{in}$ are the outer and inner diameters of the tube (m). The number of fluid flow paths for the proposed solar site is assumed to be two. The total cross-sectional area of the fluid path ($A_{sec}$) in ($m^2$) is related to the total mass flow rate, the density and the proposed tube fluid velocity of the HTF. Equation (17) describes the relation between these parameters:

$$A_{sec} = \frac{\dot{m}_{total}}{\rho_{ms} \times v_{tube}} \tag{17}$$

where $\rho_{ms}$ is the density of the molten salt HTF (kg/m$^3$) and $v_{tube}$ is the HTF velocity inside the tube (m/s). The HTF velocity ($v_{tube}$) is selected to meet the required mass flow rate inside a tube. Then it is important to assume a realistic value for the fluid speed to define the interior geometry of the receiver. However, due to the confidentiality of this type of information, a rule of thumb is used to assume the value of $v_{tube}$. The velocity of the fluid in the receiver tube for the Gemasolar power plant is close to 2.8 m/s [23]. Thus, this value is used as a first assumption.

Then, the number of tubes per header can be computed by Equation (18):

$$n_{tubes/header} = \frac{A_{sec}}{\frac{\pi}{4} {d_{in}}^2 \times n_{flow\ path}} \tag{18}$$

where $d_{in}$ is the inner diameter of the receiver tube (m) and $n_{flow\ path}$ is the designed number of the flow path and is equal to 2. To find the number of headers in a receiver, first the length of one header is required to be calculated. The length of a header can be approximated in Equation (19):

$$\text{Header length} = \text{dout} \times n_{tubes/header} + (1.2e-3 \times (n_{tubes/header} - 1)) \tag{19}$$

where $d_{out}$ is the outer diameter of the tube receiver (m), $1.2 \times 10^{-3}$ is an approximate weld thickness (m), and $(n_{tubes/header} - 1)$ is the number of gaps between tubes in a header. Then, the number of headers for a receiver can be expressed in Equation (20):

$$n_{header/receiver} = \frac{\pi \times D_{re}}{\text{Header length}} \tag{20}$$

where $D_{re}$ is the diameter of the receiver (m). It is important to note that the number of headers per receiver must be a multiple of 2 because the receiver has been desgined with two parallel flow paths. Therefore, the number of headers can be distributed equally per receiver side. Finally, once the number of tubes per header and the number of headers per receiver are calculated, the total number of receiver tubes ($n_{tubes,total}$) can be calculated by Equation (21):

$$n_{tubes,total} = n_{tubes/header} \times n_{header/receiver}. \tag{21}$$

3.7.2. Receiver Thermal Efficiency

It is recognised that an unsteady-state mathematical model for calculating thermal receiver efficiency can give a more accurate result in defining the optimum geometry of an external receiver. However, this would complicate the designing process [20]. Therefore, a steady-state mathematical model was used to compute the thermal performance of the receiver. The first law of thermodynamics (energy balance) was used to analyses the thermal performance of the receiver. This states that "the total energy of an isolated system is constant; energy can be transformed from one form to another, but can be neither created nor destroyed". Therefore, the total energy balance equation for the body of the receiver can be described by Equation (22):

$$Q_{re} = Q_{abs} + Q_{loss,total} \tag{22}$$

where $Q_{loss,total}$ (W) is the total heat transfer losses, which include convection, emmisive, reflective and conduction heat losses. The total heat losses can be stated using Equation (23):

$$Q_{loss,total} = Q_{conv,air} + Q_{em} + Q_{ref} + Q_{cond}. \tag{23}$$

The energy balance model for a receiver tube can be illustrated as shown in Figure 9, where $r_{in}$ and $r_{out}$ are the inner and outer radius of a tube (m), respectively.

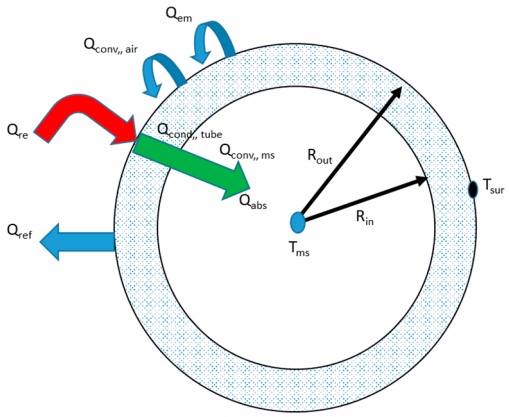


**Figure 9.** Energy balance model for a receiver tube.

Then, thermal efficiency of the external receiver can be computed by Equation (24):

$$\eta_{re} = \frac{Q_{abs}}{Q_{re}} = 1 - \frac{Q_{loss,total}}{Q_{re}} \quad (24)$$

To compute the receiver efficiency, total heat losses need to be calculated, which depend on the average receiver surface temperature. Therefore, it is necessary to discern the receiver surface temperature to calculate receiver efficiency.

### 3.7.3. Receiver Surface Temperature

The receiver surface temperature depends on the amount of incident solar radiation on the receiver surface and the temperature of the HTF that runs through the tubes. It is assumed that the receiver has a uniform surface temperature. Therefore, the present thermal analysis takes account of thermal performance of a single tube. Thermal resistance circuit for a receiver tube is shown in Figure 10.

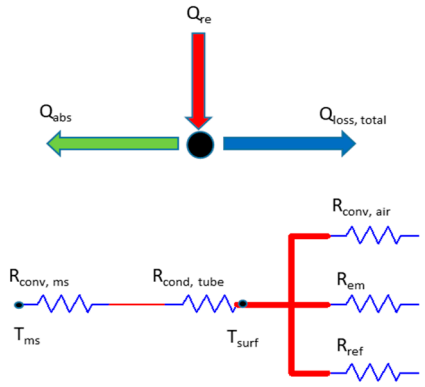


**Figure 10.** Thermal resistance circuit diagram of a receiver tube.

Based on the above thermal circuit, the receiver surface temperature can be determined by Equation (25):

$$Q_{abs,tube} = \frac{1}{R_{total}} \times (T_{surf} - T_{ms}) \quad (25)$$

The absorbed thermal energy per tube ($Q_{abs,tube}$ in W) has been used, as this analysis is based on the thermal performance of a tube. Then, the total thermal resistance ($R_{total}$ in K/W) for a tube is the sum of the conduction resistance ($R_{cond,tube}$) between the outer and inner surface of the tube and the convection resistance ($R_{conv,ms}$) between the inner wall of the tube and the HTF. The mean temperature

of the molten salt fluid ($T_{ms}$) can be calculated as in Equation (6). The conduction resistant of a tube can be written as shown in Equation (26):

$$R_{cond,tube} = \frac{\ln \frac{r_{out}}{r_{in}}}{2 \times \pi \times H_{re} \times k_{tube}} \quad (26)$$

where $H_{re}$ is the height of the receiver (in m) and $k_{tube}$ is the thermal conductivity of the receiver tube (in W/(m·K). A 316 stainless steel tube is used in this desgin ($k_{tube}$ = 23.9 W/m·K). The convection resistance inside the tube is expressed in Equation (27):

$$R_{conv,ms} = \frac{1}{h_{ms} \times \pi \times r_{in} \times H_{re}} \quad (27)$$

In the Equation (28), $h_{ms}$ is the molten salt convection heat transfer coefficient in the tube (W/m$^2$ K), which can be calculated by Equation (28):

$$Nu_{ms} = \frac{h_{ms} \times k_{ms}}{D_{in}} \quad (28)$$

where $k_{ms}$ is the thermal conductivity of the molten salt and the molten salt is assumed to be constant (0.45 W/m·K). Due to the fluid velocity inside the tube ($v_{tube}$), the flow in the tube is kept in full turbulent flow conditions, where Re > 10,000. This is to avoid any freezing for the HTF inside the tube, which could damage the receiver. Therefore, the Gnielinski equation (Equation (29)) is used to give an accurate result for the Nusselt number [21]:

$$Nu_{ms} = \frac{\left(\frac{f}{8}\right) \times (Re_{ms} - 1000) \times Pr_{ms}}{1 + 12.7 \times \left(\frac{f}{8}\right)^{0.5} \times \left(Pr_{ms}^{\frac{2}{3}} - 1\right)}, \; 0.5 \le Pr_{ms} \le 2000, 3 \times 10^3 \le Re_{ms} \le 5 \times 10^6 \quad (29)$$

The Reynolds number ($Re_{ms}$) and the Prandtl number ($Pr_{ms}$) for the thermal proprieties of HTF need to be calculate at the mean temperature of the fluid Tms, and then $Re_{ms}$ $Pr_{ms}$ can be computed by Equations (30) and (31):

$$Re_{ms} = \frac{\rho ms \times v_{tube} \times D_{in}}{\mu ms} \quad (30)$$

$$Pr_{ms} = \frac{\mu ms \times Cp_{ms}}{kms} \quad (31)$$

For smooth tubes, the friction factor in turbulent flow can be calculated from the first Petukhov equation [20], as described in Equation (31):

$$f = (0.790 \times \ln Re_{ms} - 1.64)^{-2}, \; 1 \times 10^4 \le Rems \le 1 \times 10^6 \quad (32)$$

The absorbed thermal energy ($Q_{abs,tube}$) can be determined in Equation (33):

$$Q_{abs,tube} = \dot{m}_{tube} \times Cp_{ms} \times (T_{out,ms} - T_{in.ms}) \quad (33)$$

The mass flow rate per tube is related to the type of flow pattern selected. The mass flow rate inside a tube can be computed by Equation (34):

$$\dot{m}_{tube} = \frac{\dot{m}_{total}}{n_{flow\ path} \times n_{tubes/header}} \quad (34)$$

Then, fluid velocity inside the tube can be calculated by using Equation (35):

$$v_{tube} = \frac{\dot{m}_{tube}}{\rho_{ms} \times A_{sec,tube}} \quad (35)$$

where $A_{sec,tube}$ is the inner cross-sectional area of the tube, see Equation (36):

$$A_{sec,tube} = \frac{\pi}{4} \times din^2 \quad (36)$$

The calculated fluid velocity should give the same result as the selected velocity. This could prove that the amount of mass flow rate per tube is correct and then can be used to define the absorbed thermal energy per tube.

### *3.8. Receiver Thermal Energy Losses*

The external receiver is exposed to three main heat losses: convection, emissive and reflection heat losses. Conduction heat loss is the smallest part of heat loss, which is generally neglected in thermal energy loss calculations. The following subsections describe main types of heat loss.

#### 3.8.1. Convection Heat Loss

In the external receiver, the convection heat loss ($Q_{conv,air}$) occurs due to the convection loss between the external body of the receiver and the surrounding air flow field [24]. The total convection losses for a cylindrical receiver can be stated as shown in Equation (37):

$$Q_{conv,air} = h_{total} \times A_{re} \times (T_{surf} - T_{amb}) \quad (37)$$

where $h_{total}$ is the total convection heat coefficient (W/m$^2$·K), which takes into account the natural $h_{nc}$ and forced $h_{fc}$ convection heat coefficients. The average ambient temperature $T_{amb}$ for the proposed site is assumed to be constant (25 °C).

Siebers and Kraabel in [25] recommended a correlation to define the total convection heat coefficient for an external receiver. This relation has been used widely among receiver designers. The recommended correlation is shown in Equation (38):

$$h_{total} = \left( {h_{nc}}^{3.2} + {h_{fc}}^{3.2} \right)^{1/3.2} \quad (38)$$

#### 3.8.2. Forced Convection Coefficient

The forced convection heat loss has a direct relationship with wind speed (m/s) and the roughness of the receiver surface. Literally, predicting the forced convection loss for an external receiver is a complicated process because the air flow over the cylindrical shape of the receiver exhibits a complex flow pattern [26]. As a result, many empirical correlations have been generated for estimating the average Nusselt number, which is used later to compute the forced convection coefficient. An estimate of roughness of a cylindrical receiver surface according is provided in Equation (39) [26]:

$$\text{Surface roughness} = \frac{r_{out}}{D_{re}} \quad (39)$$

where $r_{out}$ is the radius of the tube receiver (in m) and $D_{re}$ is the receiver diameter (in m).

Then, according to the assumed wind velocity (8 m/s) and the estimated surface roughness ($r_{out}/D_{re} = 300 \times 10^{-5}$), Equation (40) is selected to calculate $Nu_D$:

$$Nu_D = 0.0135 \times {Re_D}^{0.89}, \; 1.8 \times 10^5 \leq ReD \leq 4.0 \times 10^6 \quad (40)$$

The Reynolds number with receiver diameter $D_{re}$, as a characteristic length, and the air thermo-physical proprieties taken at the film temperature ($T_{fm}$ K) can be worked out as in Equations (41) and (42). Suitable correlations to define air thermal properties at the film temperature are shown in Table 2.

$$Re_D = \frac{\rho_{air} \times v_{wind} \times D_{in}}{\mu_{air}} \tag{41}$$

$$T_{fm} = \frac{T_{surf} + T_{amb}}{2} \tag{42}$$

**Table 2.** Correlations for the dry air theoretical physical properties.

| Property | Correlation |
|---|---|
| Fluid density (ρ), [kg/m$^3$] | $\rho_{air} = \frac{351.99}{T_{fm}} + \frac{344.84}{{T_{fm}}^2}$ |
| Specific heat capacity, [J/(kg.K)] | $Cp_{air} = 1030.5 - 0.19975 \times T_{fm} + 3.9734 \times 10^{-4} \times {T_{fm}}^2$ |
| Dynamic viscosity [$10^{-6}$ Pa.s] | $\mu_{air} = \frac{1.4592 \times {T_{fm}}^{3/2}}{109.10 + T_{fm}}$ |
| Thermal conductivity [W/(m.K)] | $k_{air} = \frac{2.3340 \times 10^{-3} \times {T_{fm}}^{3/2}}{164.54 + T_{fm}}$ |

The forced convection coefficient ($h_{fc}$) is computed according to Equation (43):

$$h_{fc} = \frac{Nu_D \times D_{re}}{k_{air}} \tag{43}$$

where $Nu_D$ is the average Nusselt number, $D_{re}$ is the receiver diameter (in m), and $k_{air}$ is the thermal conductivity of the air (in W/m·K).

3.8.3. Natural Convection Coefficient

The primary cause for natural convection heat loss occurring in the external receiver is the buoyancy force which is introduced by replacing the heated air in the vicinity of the receiver by cooler air nearby [26]. In natural convection analysis, the external receiver can be treated as a vertical plate because the receiver diameter is significantly large, and then the curvature effects can be neglected. The receiver diameter satisfies condition described by Equation (44):

$$D_{re} \geq \frac{35 \times H_{re}}{Gr_H} \tag{44}$$

where $Gr_H$ is the Grashof number dimensionless parameter for the receiver height ($H_{re}$) as a characteristic length. Grashof number $Gr_H$, can be calculated using Equation (45):

$$Gr_H = \frac{g \times \beta \times (T_{surf} - T_{amb}) \times H_{re}}{v} \tag{45}$$

where g is the gravitational acceleration (m/s$^2$), β is the coefficient of volume expansion (1/$T_{fm}$ 1/K), and v is the kinematic viscosity of the air (m$^2$/s).

Then, to find the average Nusselt number for natural convection over a vertical plate, the Churchill and Chu correlation is used. Although this equation is complex, it can lead to more accurate results. The correlation for $Nu_H$ is described by Equation (46):

$$Nu_H = \left\{0.825 + \frac{0.387 \times {Ra_H}^{1/6}}{\left[1 + \left(\frac{0.492}{Pr}\right)^{\frac{9}{16}}\right]^{\frac{8}{27}}}\right\}^2 \tag{46}$$

where $Ra_H$ is the Rayleigh number, which is the product of the Grashof number ($Gr_H$) and the Prandtl number (Pr). The Prandtl number for the air required is computed at the film temperature $T_{fm}$ by Equation (47):

$$Pr_{air} = \frac{\mu_{air} \times Cp_{air}}{k_{air}} \quad (47)$$

After the Nusselt number is calculated, the natural convection coefficient can be determined by Equation (48):

$$h_{nc} = \frac{Nu_H \times H_{re}}{k_{air}} \quad (48)$$

3.8.4. Conduction Heat Loss

Conduction heat loss ($Q_{cond}$) is the smallest part of the total heat losses and occurs due to conduction in the insulation layer. Most receiver design reports have neglected this type of heat loss [20] determined the conduction heat loss as shown in Equation (49):

$$Qcond = \frac{(T_{surf} - T_{ins,w})}{\frac{k_{ins}}{t_{ins}}} \times A_{re} \quad (49)$$

where $T_{ins,w}$ is the temperature at the insulation surface (in K), $k_{ins}$ is the thermal conductivity of the insulation layer (in W/m·K), and $t_{ins}$ is the insulation layer thickness. The temperature at the insulation surface is required to complete the analysis. In an experimental analysis approach, this value can be measured and then used in the rest of the calculation. However, in a mathematical analysis, this temperature needs to be assumed, which can lead to incorrect results. The current analysis does not consider conduction heat loss in the insulation layer.

3.8.5. Emissive Heat Loss

Emissive heat loss occurs due to infrared radiation, which is emitted from the external receiver wall. The external body of the receiver is treated as a grey surface, to be independent of the wavelength. In general, a black coating is applied on the external wall of the receiver. Then, total emissive heat loss can be computed using Equation (50):

$$Q_{em} = \varepsilon \times \sigma \times A_{re} \times \left({T_{surf}}^4 - {T_{amb}}^4\right) \quad (50)$$

where $\varepsilon$ is the emissivity of coating surface and $\sigma$ is the Stefan-Boltzmann constant ($5.67 \times 10^{-8}$, $W/m^2 \cdot K^4$).

3.8.6. Reflective Heat Loss

Reflective heat loss exists due to the reflectivity of the receiver material, which is intended for an opaque surface, Equation (51):

$$\text{Reflectivity} = 1 - \alpha \quad (51)$$

where $\alpha$ is the surface absorptivity thus, the reflection heat loss $Q_{ref}$ (W) for an external receiver is calculated by Equation (52):

$$Q_{ref} = (1 - \propto) \times Q_{re} \quad (52)$$

The surface temperature and heat loss model was built in Simulink a shown in Figure 11a,b. The model calculates the receiver temperature for a range of receiver geometries. Then, the results of this model are used to calculate total thermal heat losses and then to define the thermal efficiency for each proposed geometry. Under each heat loss type, the mathematical equations are transferred into the Simulink environment. Since the total heat loss is calculated, the thermal efficiency for the proposed receiver geometry can be calculated.

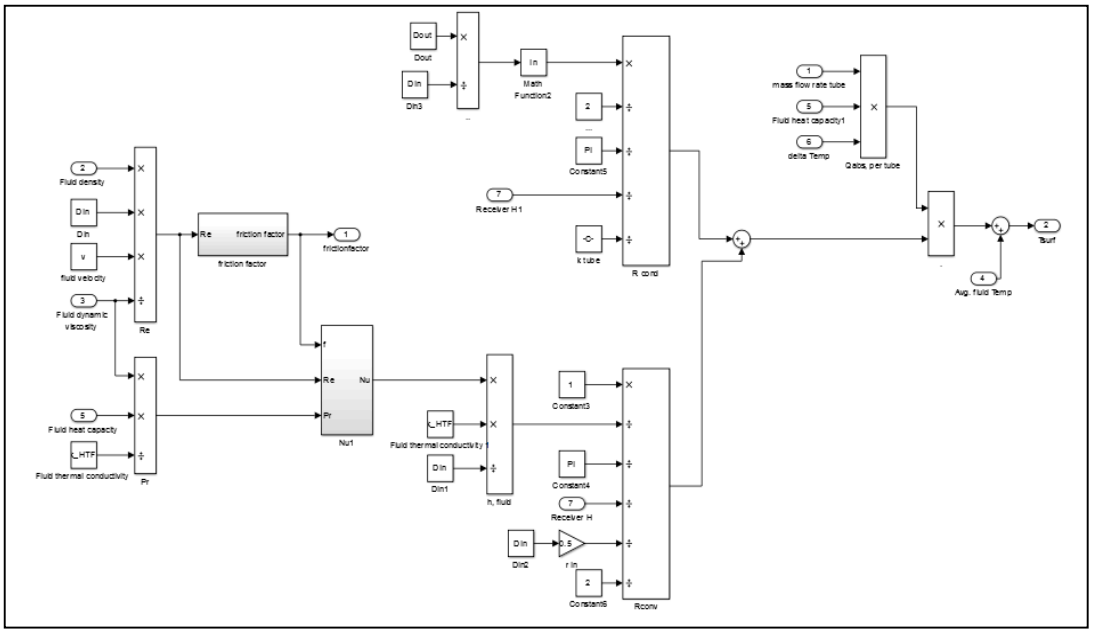


(**a**)

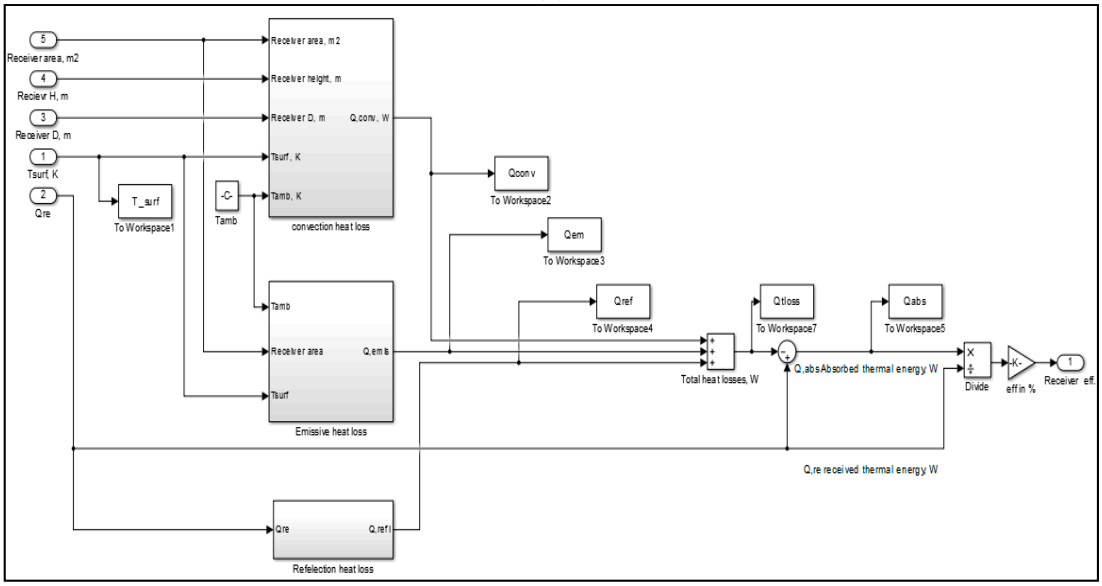


(**b**)

**Figure 11.** (**a**): Surface temperature model. (**b**): Receiver heat transfer model.

### *3.9. Pumping Power Costs*

The second parameter to define the optimum geometry of an external receiver is the cost of the required pumping power, which is the cost of the electrical energy needed to pump an HTF through a receiver. The required energy can be defined by Equation (53):

$$\dot{W}_{pump} = \frac{\dot{V} \times \Delta P_{toal}}{\eta_{pump}} \quad (53)$$

where $\dot{W}$ is the required pump power (in W), $\dot{V}$ is the volume flow rate of molten salt HTF (in $m^3/s$) and is equal to $\dot{m}_{total}/\rho_{ms}$, $\Delta P_{total}$ is the total pressure drop in Pa, and $\eta_{pump}$ is the pump efficiency and is assumed to be a constant 75%. Pressure drop occurs in a receiver due to two main factors: first,

pumping molten salt fluid to the top of a solar tower, where the receiver is located, and this can be expressed by Equation (54):

$$\Delta P_{tower} = \rho_{ms} \times g \times H_{tower} \quad (54)$$

where $H_{tower}$ is the solar tower height, which is assumed to be 140 m.

Second, pressure drop occurs due to pumping HTF through the receiver tubes, and it can be computed as in Equation (55):

$$\Delta P_{tube} = \rho_{ms} \times f \times \frac{H_{re}}{D_{in}} \times \frac{x_{tube}{}^2}{2} \quad (55)$$

where f is the fiction factor for a smooth tube in turbulent flow; see Equation (32). The total pressure drop is the sum of the tower pressure drop and the total pressure as described by Equation (56).

Annual cost of electricity for operating of the receiver pump is given in Equation (57):

$$\Delta P_{total} = \Delta P_{tube} \times \frac{n_{header/receiver}}{n_{flow\ path}} + \Delta P_{tower} \quad (56)$$

$$\text{Operating cost} = \dot{W}_{pump} \times \text{operating hours} \times \text{Price of electricty} \quad (57)$$

To simplify the operating cost analysis, it is assumed that the pump operates 9 h a day. Furthermore, the system has 20 days of shutdown maintenance per year, so the approximate annual operating hours for the receiver pump can be calculated as 3121 h. Since the proposed location for the current project is Saudi Arabia, the consumption tariff of electricity for the industrial sector is used to define the price of electricity in £/kWh. According to the Saudi Electricity Company, the price of electricity for the industrial sector is 0.04 £/kWh. Then, the cost of pumping power for different receiver geometries can be computed. Figure 12 illustrates the Simulink model of calculating the cost of pumping power for each receiver geometry.

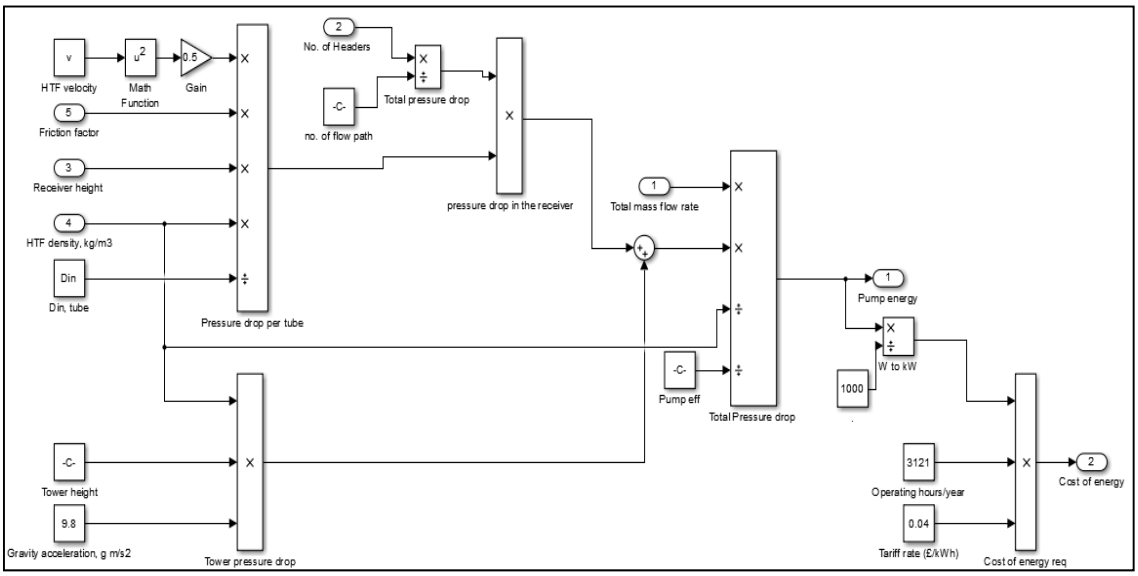


**Figure 12.** Cost of pumping power model.

### *3.10. Modelled System Parameters*

The recommended design optimisation approach for external receivers were modelled by MATLAB and Simulink software. This section outlines the main input parameters of the model and how the model is implemented are discussed. Initially, the model uses two types of parameters: fixed and variable. The fixed parameters are the design point parameters of the solar system, which are listed in Table 3.

**Table 3.** Fixed input parameters for the Simulink model.

| Properties | Value | Unit |
|---|---|---|
| System rated capacity | 20 | MWe |
| Thermal storage capacity | 15 | Hours |
| Heliostat field efficiency $\eta_h$ | 70 | % |
| Initial value for receiver efficiency $\eta_{re}$ | 85 | % |
| Power block efficiency $\eta_{tur}$ | 42 | % |
| Direct normal radiation (DNI) | 950 | $W/m^2$ |
| Wind velocity | 8 | m/s |
| Ambient temperature | 25 | °C |
| Molten salt inlet temperature | 290 | °C |
| Molten salt outlet temperature | 565 | °C |
| Molten salt density $\rho_{ms}$ | 1818 | $Kg/m^3$ |
| Molten salt specific heat Cpms | 1517 | J/(kg K) |
| Molten salt dynamic viscosity $\mu_{ms}$ | 0002125 | Pa.s |
| Molten salt thermal conductivity $k_{ms}$ | 0.45 | W/(m K) |
| Allowable heat flux | 578.23 | $kW/m^2$ |
| Fluid tube velocity | 3.3 | m/s |
| Stefan-Boltzmann constant σ | $5.67 \times 10^{-8}$ | $W/(m^2 K^4)$ |
| Pump efficiency | 75 | % |
| Tower height | 140 | m |
| Annual operating receiver pump hours | 3121 | Hour |
| Electricity tariff rates in Saudi Arabia for the industrial sector | 0.04 | £/kWh |
| Number of flow paths | 2 | |
| Coating surface emissivity | 85 | % |
| Coating surface absorptivity | 93 | % |

The value of the receiver efficiency is initially assumed with a view to defining the equivalent rated capacity of the solar system. Then, for each proposed receiver geometry, the receiver thermal efficiency is calculated and readjusted according to the total thermal energy losses.

As the aim of this research is to find the best geometric design for an external receiver, the Simulink model was used to measure the effect of different proposed receiver geometries on the thermal efficiency of the receiver and the cost of pumping energy. In addition, the model analyses the effect of material tube thermal conductivity on total thermal efficiency. The acceptable ranges for each variable are collected from different studies, see Table 4.

**Table 4.** Variable input parameters for the Simulink model.

| Properties | Range | Unit | Reference |
|---|---|---|---|
| Aspect ratio | 1–2 | | [20] |
| Tube diameter | 20–60 | mm | [27] |
| Tube thickness | 1–3 | mm | [7] |
| Tube thermal conductivity | | | |
| Stainless steel 316 | 12–45 | W/(m K) | www.engineeringtoolbox.com |
| Inconel alloy 625 | 21–100 | W/(m K) | |
| Incoloy 800 H | 0–100 | W/(m K) | |

## 4. Results and Discussion

### *4.1. Effects of Tube Diameter on Receiver's Performance*

The effect of tube diameter on external receiver performance is shown in Figure 13. The figure shows that the receiver thermal efficiency is improved when the receiver tube diameter is decreased. The improvement of receiver efficiency is due to the reduced receiver surface temperature. When receiver surface temperature is decreased, the amount of heat loss is decreased (see Figure 14).

The receiver efficiency for a tube diameter of 20 mm is approximately 86%, whereas, it is around 60% at a 60 mm tube diameter; therefore, the receiver efficiency would improve about 26% if the smaller diameter is selected. In terms of the annual pumping energy cost, no noticeable effect was observed of the tube diameter on the annual pumping energy cost. Using the smallest tube size increased the annual cost by only £36. This is probably due to change of tube diameter from 60 to 20 mm has no obvious effect on the total pressure drop on the receiver.

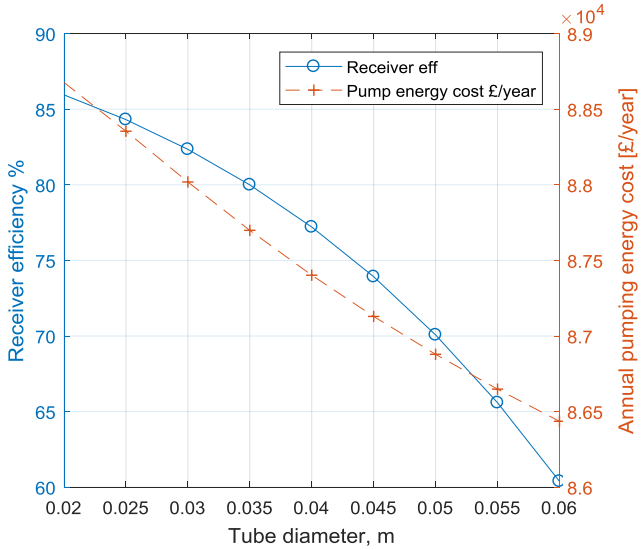


**Figure 13.** Tube diameter effects on receiver efficiency and pump energy cost.

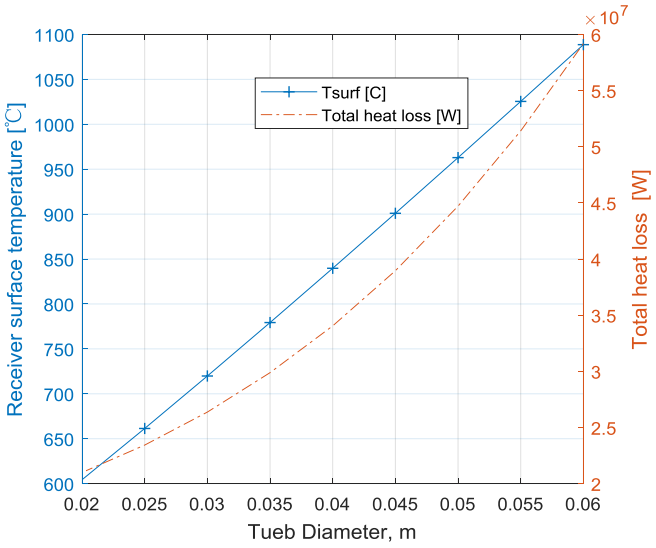


**Figure 14.** Tube diameter effects on receiver surface temperature.

Therefore, it can be concluded that a smaller receiver tube diameter can give higher receiver thermal efficiency and is preferable in designing an external receiver.

### *4.2. Effect of Tube Thickness on Receiver's Performance*

The impact of tube thickness on receiver efficiency and annual energy cost are shown in Figure 15. Two different regions for tube thickness are depicted. The first region corresponds to a tube thickness between 1 mm and 2.5 mm. In this region, the receiver efficiency decreases exponentially with increasing tube thickness. This could be explained by Figure 16, where receiver temperature increases

with the same pattern. In the second region, which is for tube thickness above 2.5 mm, the receiver efficiency starts to increase slightly. This is possibly due to the assumption of a fixed fluid speed. The fluid speed should increase when the inner tube diameter is decreased. Therefore, the effect of this assumption starts to be noticed when the tube thickness is greater than 2.5 mm. It can be concluded that the receiver efficiency at a small tube thickness is higher than at a large thickness.

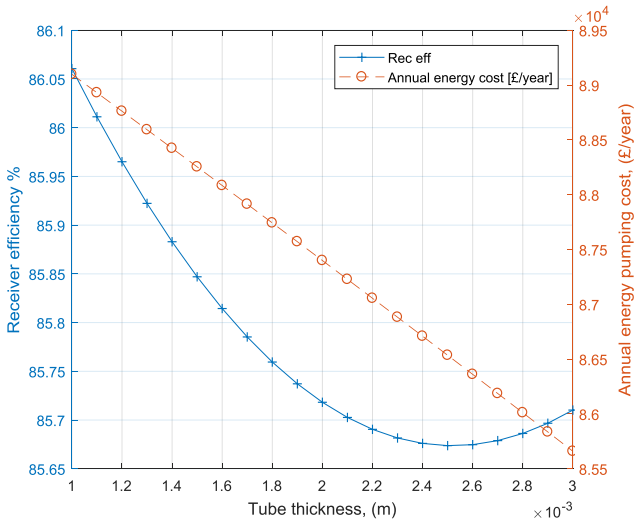


**Figure 15.** Tube thickness effects on receiver efficiency and annual energy cost.

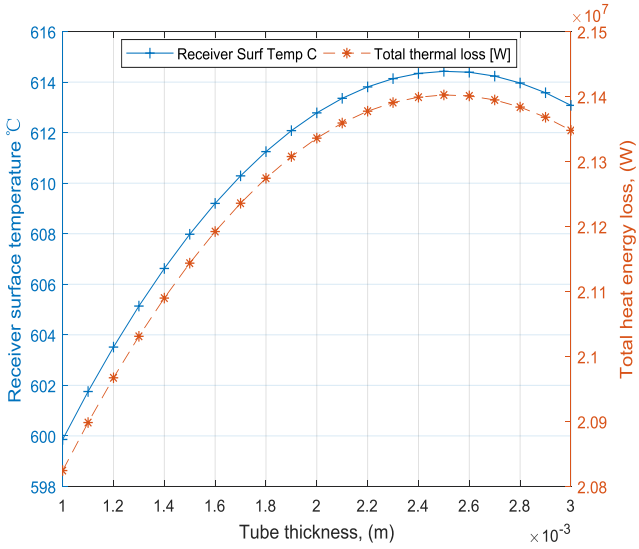


**Figure 16.** Relationship between tube thickness and receiver surface temperature.

For the energy cost analysis, the cost of pumping HTF to the receiver decreases linearly with tube thickness (Figure 16). The proposed tube thickness' range has a moderate effect on the annual cost of energy. The difference in cost between the minimum and maximum tube thickness is around £3500 per year. However, at 1 mm tube thickness, the receiver efficiency is greater than the largest tube thickness by approximately 0.4%, which equals about 600 kWth thermal energy. Then, the smallest tube thickness for a molten salt external receiver has a low heat loss and provides more thermal energy, which minimises the cost of pumping power.

### *4.3. Aspect Ratio Impacts on Receiver Performance*

The aspect ratio (AR) is the relation between the receiver height and diameter. This ratio was investigated to determine its impact on the receiver thermal performance and the annual cost of pumping energy. Figure 16 illustrates the relationship curve between receiver efficiency and the aspect ratio. The figure shows that a taller height receiver is more desirable for minimising total thermal heat losses. However, if the aspect ratio were to equal 2, the receiver diameter would decrease to around 6.5 m, which might not be enough to accommodate the interior components of the receiver. Then, an AR of 1.5 was selected to increase the receiver efficiency and, at the same time, the receiver diameter was increased to 7.5 m (Figure 17).

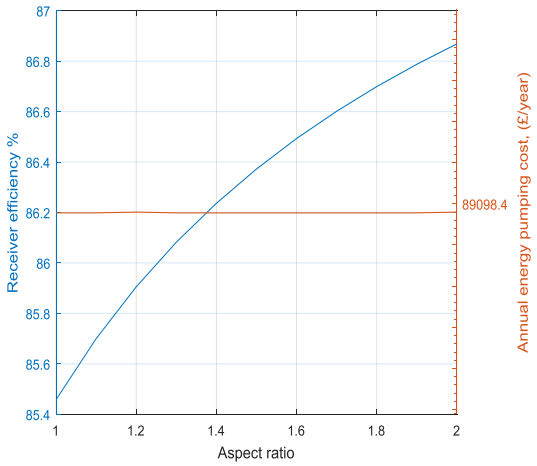


**Figure 17.** Effects of aspect ratio on receiver efficiency and annual energy cost.

Figure 18 depicts that the aspect ratio has no effect on total pumping power. A possible reason may be that the receiver surface area is constant. In that case, the total pressure drop was not affected by changing the aspect ratio.

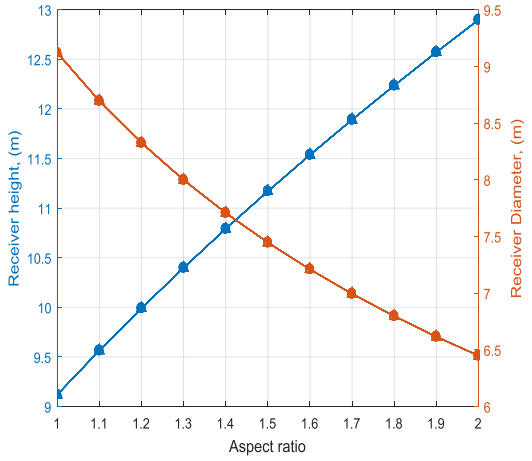


**Figure 18.** Aspect ratio vs. receiver height and diameter.

### *4.4. Tube Thermal Conductivity Effects on Receiver Performance*

As elicited from the literature review, the three main materials that are used in manufacturing receiver tubes are stainless steel 316, Inconel alloy 625 and Incoloy 800 H. The thermal conductivity and the cost associated with each material are summarised in Table 5.

**Table 5.** Thermal conductivity and material cost for common receiver tubes [3].

| Material | Thermal Conductivity W/m·K | Cost $/kg |
|---|---|---|
| Stainless steel 316 | 12–45 | 2.5–5 |
| Inconel alloy 625 | 21–100 | 20–25 |
| Incoloy 800H | 0–100 | 40–80 |

Figure 19 shows the evolution of receiver efficiency as a function of a tube's thermal conductivity. The receiver efficiency decreases sharply for a tube material that has a thermal conductivity below 6 W/m·K. However, after 28 W/m·K, the thermal conductivity of a material has no effective influence on receiver efficiency. Therefore, materials such as stainless steel 316 could be used in designing solar receivers. Although Inconel alloy 625 and Incoloy 800 H have higher thermal conductivity than stainless steel, their thermal conductivity has no effect on the thermal performance of the solar receiver. Since thermal stress analysis is out of the research scope, stainless steel 316 tube material is selected for this project due to its acceptable thermal conductivity and its low cost.

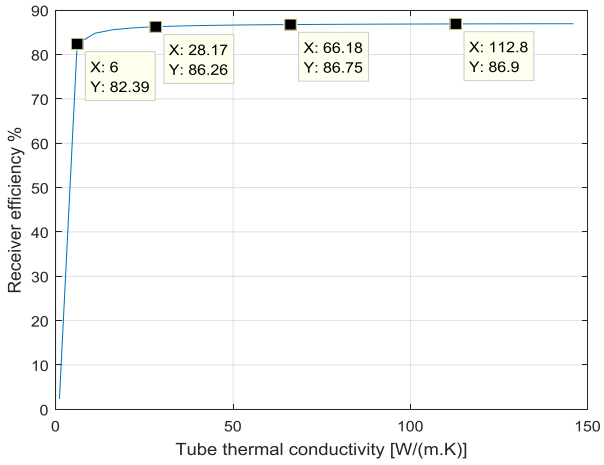


**Figure 19.** Influence of tube thermal conductivity on receiver thermal efficiency.

### *4.5. Tube Size and Thickness Fitting Analysis*

In previous sections, the optimum tube diameter and thickness were investigated according to receiver thermal efficiency and pumping cost energy. Table 6 shows the first-attempt results of the Simulink model.

**Table 6.** The output results of the first iteration.

| Input Parameters | | Output Results | |
|---|---|---|---|
| Tube diameter (mm) | 20 | Tubes/header | 100 |
| Tube thickness(mm) | 1 | Headers/receiver | 12 |
| Aspect ratio | 1.5 | Total No. of tubes | 1200 |
| - | | Receiver diameter (m) | 7.5 |
| | | Receiver height (m) | 11.3 |

However, before, we finalise these results, it is crucial to check the fitting of the selected tube size and tube thickness with the calculated outer receiver geometry. To complete this step, the maximum number of tubes for a receiver needs to be calculated according to Equation (58):

$$\text{Max No. of tubes per receiver} = \frac{\pi \times D_{re}}{d_{out}} \quad (58)$$

Maximum number of tubes per receiver is related to the tube diameter and the receiver diameter. Thus, the maximum number ($D_{re}$ = 7.5 m and $d_{out}$ = 20 mm) is approximately 1178 tubes. However, the model result for the total number of tubes is 1200 tubes, which is more than the maximum. Therefore, the next higher size of tube diameter, 25 mm, was used to decrease the total number of tubes; see Table 7. The maximum number of tubes for a 25 mm receiver tube is 942 tubes. Simulink model shows that the total number of tubes should be is 868 tubes per receiver, which is below the maximum tube number (942 tubes). Furthermore, it was observed that a small tube thickness can lead to higher receiver efficiency. Thus, a tube thickness of 1 mm was used in this simulation model.

**Table 7.** The output results of the second iteration.

| Input Parameters | | Output Results | |
|---|---|---|---|
| Tube diameter (mm) | 25 | Tubes/header | 62 |
| Tube thickness (mm) | 1 | Headers/receiver | 14 |
| Aspect ratio | 1.5 | Total No. of tubes | 868 |
| - | | Receiver diameter (m) | 7.5 |
| | | Receiver height (m) | 11.3 |

After adjusting tube diameter and thickness, the receiver efficiency and the annual cost of pumping power were recomputed as 85% and 90,721 £/year, respectively.

### *4.6. Receiver Design Validation*

Having discussed and created the mathematical model for the external solar receiver, the results of this design methodology were compared and validated using real data from a well-established reference SPT plant. The Gemasolar Thermal Plant is considered one of an only a few SPT plants that have achieved the continuous 24 h per day production of electricity. It is in the city of Fuentes de Andalucía in Seville province in Spain. This commercial solar plant was selected as a reference plant for the following reasons:

- The Gemasolar power plant uses SPT technology, which is the same technology that is proposed for this project.
- Both the solar plant and the existing model use molten salt as an HTF and as an energy storage medium.
- The rated capacity of the Gemasolar plant is nearly as same as the projected solar system. The rated capacity of Gemasolar Thermal Plant is 19.9 MWe, and the proposed project's capacity is 20 MWe.
- The reference solar plant has a thermal energy storage unit with 15 h capacity. The same thermal energy capacity is used in our model.
- Most significantly, the Gemasolar solar plant uses an external solar receiver, which is the aim of this research.

Therefore, the actual data of the Gemasolar external receiver was gathered from different studies and listed in Table 8 to be compared with the results of the Simulink model. In the table, the actual receiver area is larger than the designed receiver area. This is probably due to the different peak-to-average ratios. The current model assumed 1.47 peak-to-average ratio, which resulted in a higher heat flux on the receiver surface of around 578.23 kW/m$^2$, whereas the Gemasolar power plant used a 1.9 peak-to-average ratio. This value decreases the average solar flux on the receiver surface to approximately 445 kW/m$^2$. Therefore, a lower peak-to-average ratio can increase the solar flux concentrated on a receiver surface and reduce the amount of receiver surface area used.

Moreover, the table shows some differences in receiver diameter and height between the receivers. There are two possible explanations. The first is related to the difference in receiver surface area, as it is obvious that the receiver height and diameter are directly related to the receiver area. The second

factor is due to the aspect ratio that is used. The proposed model used a 1.5 aspect ratio, and the Gemasolar receiver used 1.25.

In terms of tube diameter, the model shows that a 25 mm tube diameter is the optimum size for a tube. This value matches the reference data. A clear understanding of the fluid flow in the receiver and the accurate estimation for the fluid velocity inside the tube led to these identical results. However, the current model proves that a small tube thickness can improve the thermal efficiency of the receiver. Therefore, a 1 mm tube thickness was selected. In addition, the number of tubes per header and per receiver is influenced by the tube diameter and thickness. The current model uses fewer tubes, which reduces the material cost by approximately $17,225. The material cost per tube is given as follows:

$$\text{Material cost per tube} = \left(\rho_{\text{tube}} \times \left({d_{\text{out}}}^2 - {d_{\text{in}}}^2\right) \times H_{\text{re}} \times \frac{\pi}{4000}\right) * \text{material cost}\left(\frac{\$}{\text{kg}}\right) \quad (59)$$

where $\rho_{\text{tube}}$ = the tube material density (in g/cm$^3$), $d_{\text{out}}$ & $d_{\text{in}}$ = the outer and inner tube diameters (in mm), and $H_{\text{re}}$ = the receiver height (in m). The material cost for the 316 stainless steel was assumed (3.75$/kg).

**Table 8.** Comparison of receiver parameters between the Gemasolar receiver and the Simulink model receiver.

| Receiver Parameters | Unit | Gemasolar Thermal Plant | Reference | Simulink Model |
|---|---|---|---|---|
| Outer Geometry | | | | |
| Total receiver area ($A_{re}$) | m$^2$ | 270 | Reference [3] | 261.2 |
| Receiver Diameter ($D_{re}$) | m | 10.6 | | 11.3 |
| Receiver Height ($H_{re}$) | m | 8.1 | | 7.5 |
| Inner Geometry | | | | |
| Tube diameter ($d_{out}$) | mm | 25 | Reference [3] | 25 |
| Tube thickness (t) | mm | 1.65 | | 1 |
| No. of tubes/headers | | 64 | Reference [19] | 62 |
| No. of headers/receivers | | 16 | | 14 |
| Total No. of tubes | | 1024 | | 868 |
| Calculated Results | | | | |
| Receiver thermal efficiency | % | 84 | Simulink model | 85 |
| The annual cost of pumping energy | £/year | 89,242 | | 90,721 |
| Total cost of tube material | $ | 39,424 | | 22,199 |

Nevertheless, the results of the table present an improvement in the thermal efficiency of the designed model of 1%. The current model absorbs thermal energy at a greater rate than Gemasolar receiver by approximately 2.69 MWth of thermal energy per hour. This will increase the output power of the solar tower system 1.13 MWe per hour, with the assumption of 42% net efficiency for the power block.

Finally, due to the small difference in the cost of pumping energy, the higher cost associated with the new design can be neglected. The difference was only about 1479 £/year.

## 5. Conclusions

In Saudi Arabia, where solar energy is in abundance, using SPT technology will boost the national energy mix plan for 2032. The optimal geometry for an external receiver used for a SPT plant was investigated in detail. A mathematical thermal model for the receiver was developed using MatLab and Simulink software. The thermal model was created based on energy balance analysis. Furthermore, the performance of the developed SPT was examined under NEOM's city metrological conditions and the annual cost associated with pumping molten salt fluid was analysed. The result of the model was compared with a well-established solar tower system. Tube diameter and tube thickness showed an inverse effect on receiver efficiency, where the aspect ratio displayed a direct effect on receiver efficiency. Both tube diameter and tube thickness have a counter-relationship with the annual cost of pumping

energy. However, for a fixed receiver surface area, the aspect ratio has no effect on the annual cost because the total pressure drop on the receiver remains constant for each aspect ratio. The incremental increase in the pumping cost, which resulted from using a small tube size, can be neglected when it is compared with the amount of thermal energy absorbed. A thermal conductivity of 28 W/m·K for a receiver tube was found to be the threshold point for receiver efficiency. Any further increase above this thermal conductivity would not have any noticeable effect on the receiver efficiency. Then, a cheaper tube material, such as 316 stainless steel, could be an adequate choice for the external receiver. Although the new receiver design has fewer tubes per receiver, it can produce 1% more thermal energy than the receiver at the Gemasolar plant can. In addition, the total cost of the tube material for the new design was reduced by approximately 43%. The validation process for the thermal model confirmed the reliability of the model for designing an external receiver type. Therefore, the proposed design of the cylindrical receiver offers more efficient and cost-effective architecture to adopt for solar power plants in hot countries, especially, KSA.

**Author Contributions:** All authors contributed equally to the research described in this work. This applies to all publication stages including research ideas, methodology, modelling, collecting experimental data, analysis of results and drafting the paper.

**Funding:** Part of the presented work was supported by the Cultural Bureau of the Kingdom of Saudi Arabia Embassy in London, UK, under project 6E7Z2120/15092176.

**Conflicts of Interest:** The authors declare no conflict of interest.

## References

1. Alyahya, S.; Irfan, A.M. The techno-economic potential of Saudi Arabia's solar industry. *Renew. Sustain. Energy Rev.* **2016**, *55*, 697–702. [CrossRef]
2. Romero, M.; Steinfeld, A. Concentrating solar thermal power and thermochemical fuels. *Energy Environ. Sci.* **2012**, *5*, 9234–9245. [CrossRef]
3. Li, X.; Kong, W.; Wang, Z.; Chang, C.; Bai, F. Thermal model and thermodynamic performance of molten salt cavity receiver. *Renew. Energy* **2010**, *35*, 981–988. [CrossRef]
4. Yang, M.; Yang, X.; Yang, X.; Ding, J. Heat transfer enhancement and performance of the molten salt receiver of a solar power tower. *Appl. Energy* **2010**, *87*, 2808–2811. [CrossRef]
5. Rodriguez-Sanchez, M.R.; Sanchez-Gonzalez, A.; Marugan-Cruz, C.; Santana, D. New designs of molten-salt tubular-receiver for solar power tower. *Energy Proced.* **2014**, *49*, 504–513. [CrossRef]
6. Edem, K.; Azoumah, K.; Ramde, E.; Yesuenyeagbe, A.; Neveu, P.; Py, X.; Gaye, M.; Jourdan, A. Integrated design and construction of a micro-central tower power plant. *Energy Sustain. Dev.* **2016**, *31*, 1–13.
7. Abu-Hamdeh, N.H.; Alnefaie, K. Design considerations and construction of an experimental prototype of concentrating solar power tower system in Saudi Arabia. *Energy Convers. Manag.* **2016**, *117*, 63–73. [CrossRef]
8. Benoit, H.; Spreafico, L.; Gauthier, D.; Flamant, G. Review of heat transfer fluids in tube-receivers used in concentrating solar thermal systems: Properties and heat transfer coefficients. *Renew. Sustain. Energy Rev.* **2016**, *55*, 298–315. [CrossRef]
9. Zheng, H.; Yu, X.; Su, Y.; Riffat, S.; Xiong, J. Thermodynamic analysis of an idealised solar tower thermal power plant. *Appl. Therm. Eng.* **2015**, *81*, 271–278. [CrossRef]
10. Wang, K.; He, Y. Thermodynamic analysis and optimization of a molten salt solar power tower integrated with a recompression supercritical CO2 Brayton cycle based on integrated modeling. *Energy Convers. Manag.* **2017**, *135*, 336–350. [CrossRef]
11. Andika, R.; Kim, Y.; Yoon, S.; Kim, D.; Choi, J.; Lee, M. Techno-economic assessment of technological improvements in thermal energy storage of concentrated solar power. *Sol. Energy* **2017**, *157*, 552–558. [CrossRef]
12. Prieto, C.; Rodríguez-Sánchez, A.; Ruiz-Cabañas, F.; Cabeza, L. Feasibility study of freeze recovery options in parabolic trough collector plants working with molten salt as heat transfer fluid. *Energies* **2019**, *12*, 2340. [CrossRef]

13. Lifeng, L.; Coventry, J.; Bader, R.; Pye, J.; Lipiński, W. Optics of solar central receiver systems: A review. *Opt. Express* **2016**, *24*, A984–A1007.
14. Mehos, M.; Turchi, C.; Vidal, J.; Wagner, M.; Ma, Z.; Ho, C.; Kolb, W.; Andraka, C.; Kruizenga, A. Concentrating Solar Power: Gen3 Demonstration Roadmap. Technical Report NREL/TP-5500-67464; 2017. Available online: https://www.nrel.gov/docs/fy17osti/67464.pdf (accessed on 29 July 2019).
15. Mokri, A.; Ali, M.; Emziane, M. Solar energy in the United Arab Emirates: A review. *Renew. Sustain. Energy Rev.* **2013**, *28*, 340–375. [CrossRef]
16. Natsheh, E.; Albarbar, A. Solar power plant performance evaluation: simulation and experimental validation. *Phys.* **2012**, *364*, 111–123. [CrossRef]
17. Vignarooban, K.; Xu, X.; Arvay, A.; Hsu, K.; Kannan, A.M. Heat transfer fluids for concentrating solar power systems—A review. *Appl. Energy.* **2015**, *146*, 383–396. [CrossRef]
18. Siva, R.; Kaushik, S.C.; Ranjan, K.R.; Tyagi, S.K. State-of-the-art of solar thermal power plants—A review. *Renew. Sustain. Energy Rev.* **2013**, *27*, 258–273. [CrossRef]
19. Falcone, P.K. A Handbook for Solar Central Receiver Design. *J. Chem. Inf. Model* **1986**, *53*, 1689–1699.
20. Wagner, M.; Klein, S.; Reindl, D. Simulation of Utility-Scale Central Receiver System Power Plants. In Proceedings of the 3rd International Conference on Energy Sustainability, ASME, San Francisco, CA, USA, 19–23 July 2009; pp. 1–10.
21. Serrano-López, R.; Fradera, J.; Cuesta-López, S. Molten salts database for energy applications: Chemical Engineering and Processing. *Process Intensif.* **2013**, *73*, 87–102. [CrossRef]
22. Zavoico, A.B. *Solar Power Tower—Design Basis Document*; Sandia National Laboratories: San Francisco, CA, USA, 2001; SAND2001–2100.
23. Marugán-Cruz, C.; Sánchez-Delgado, S.; Rodríguez-Sánchez, M.; Venegas, M.; Santana, D. District cooling network connected to a solar power tower. *Appl. Therm. Eng.* **2015**, *79*, 174–183. [CrossRef]
24. NREL Concentrating Solar Power Projects. Professional Report. Available online: https://www.nrel.gov/csp/solarpaces/by_country_detail.cfm/country=SA (accessed on 29 July 2019).
25. Siebers, D.; Kraabel, J. Estimating convective energy losses from solar central receivers. *Tech. Rep.* **1984**. [CrossRef]
26. Sánchez, M. On the Design of Solar External Receivers. Ph.D. Thesis, University Carlos Madrid, Madrid, Spain, 2015.
27. Natsheh, E.; Natsheh, A.; Albarbar, A. Intelligent controller for managing power flow within standalone hybrid power systems. *IET Sci. Meas. Technol.* **2013**, *7*, 191–200. [CrossRef]